

# Interweaving Polar Charge Orders in a Layered Metallic Superatomic Crystal

Shuya Xing,<sup>1,||</sup> Linlu Wu,<sup>1,||</sup> Zilu Wang,<sup>1,||</sup> Xu Chen,<sup>2,||</sup> Haining Liu,<sup>3,4</sup> Shuo Han,<sup>1</sup> Le Lei,<sup>1</sup> Linwei Zhou,<sup>1</sup> Qi Zheng,<sup>2,4</sup> Li Huang,<sup>2,4</sup> Xiao Lin,<sup>4</sup> Shanshan Chen,<sup>1</sup> Liming Xie,<sup>3,4</sup> Xiaolong Chen,<sup>2,4,5</sup> Hong-Jun Gao,<sup>2,4</sup> Zhihai Cheng,<sup>1,\*</sup> Jiangang Guo,<sup>2,5,†</sup> Shancai Wang,<sup>1,‡</sup> and Wei Ji<sup>1,§</sup>

<sup>1</sup>Beijing Key Laboratory of Optoelectronic Functional Materials and Micro-nano Devices, Department of Physics, Renmin University of China, Beijing 100872, China

<sup>2</sup>Beijing National Laboratory for Condensed Matter Physics, Institute of Physics, Chinese Academy of Sciences, P.O. Box 603, Beijing 100190, China

<sup>3</sup>CAS Key Laboratory of Standardization and Measurement for Nanotechnology, CAS Centre for Excellence in Nanoscience, National Centre for Nanoscience and Technology, Beijing 100190, China

<sup>4</sup>University of Chinese Academy of Sciences, Beijing 100039, China

<sup>5</sup>Songshan Lake Materials Laboratory, Dongguan, Guangdong 523808, China



(Received 17 February 2022; revised 8 September 2022; accepted 3 October 2022; published 26 December 2022; corrected 13 September 2023)

Electronic properties of superatomic crystals have not been sufficiently explored due to the versatility of their building units; moreover, their interunit couplings are even poorly understood. Here, we present a joint experiment-theory investigation of a rationally designed layered superatomic crystal of  $\text{Au}_6\text{Te}_{12}\text{Se}_8$  (ATS) cubes stacked by noncovalent intercubane quasibonds. We find a sequential-emerged anisotropic triple-cube charge density wave (TCCDW) and polarized metallic states below 120 K, as revealed via scanning tunneling microscopy and spectroscopy, angle-resolved photoemission spectroscopy, transport measurement, Raman spectra, and density-functional theory. The polarized states are locked in an antiparallel configuration, which is required for maintaining the inversion symmetry of the center cube in the TCCDW. The antipolar metallic states are thus interweaved by the CDW and the polarized metallic states, and primarily ascribed to electronic effects via theoretical calculations. This work not only demonstrates a microscopic picture of the interweaved CDW and polarized charge orders in the superatomic crystal of ATS, but also sheds light on expanding the existing category of quantum materials to noncovalent solids.

DOI: [10.1103/PhysRevX.12.041034](https://doi.org/10.1103/PhysRevX.12.041034)

Subject Areas: Condensed Matter Physics, Materials Science

## I. INTRODUCTION

The pioneering synthesis of emergent crystals, e.g., iron-based superconductors ( $\text{La}[\text{O}_{1-x}\text{F}_x]\text{FeAs}$ ) [1], perovskite solar cells ( $\text{CH}_3\text{NH}_3\text{PbI}_3$  [2,3] and  $\text{CH}_3\text{NH}_3\text{PbBr}_3$  [4]), and two-dimensional magnetism ( $\text{CrI}_3$ ) [5–7], has always attracted significant attention among researchers. In particular, these crystals have been useful in discovering novel physical phenomena in materials science, exploring intriguing properties, and unraveling unexplored principles. The subsequent optimization of these crystals, e.g.,

$\text{La}[\text{O}_{1-x}\text{F}_x]\text{FeAs}$ , by altering one type of atom with another was limited due to the fact that only 82 stable and nonradioactive elements could be used, and each of them has its own bonding characteristics which are largely different from each other. Thus, substituting a new type of atom into a given material typically introduces different structures with widely varying properties [8–10]. This, however, poses an overwhelming challenge to rationally designing functional materials [11,12].

Stacking two-dimensional (2D) monolayers through noncovalent van der Waals (vdW) interactions between layers offers a new means to overcome the aforementioned challenge. In fact, vdW attractions in the stacked 2D materials usually introduce interlayer wave-function overlaps with subsequent electronic hybridization. This is known as the covalentlike quasibonding (CLQB) because the overlapped wave functions yield a covalentlike charge redistribution characteristic at the interlayer region [13–16]. Exploiting CLQB is an interesting approach to introducing substantial changes to band gaps [13,14], optical transitions [15,16], topological properties [17], magnetism [18,19], electrical polarization [20], and superconductivity [10,21],

\*zhihaicheng@ruc.edu.cn

†jgguo@iphy.ac.cn

‡scw@ruc.edu.cn

§wji@ruc.edu.cn

||These authors contributed equally to this work.

Published by the American Physical Society under the terms of the [Creative Commons Attribution 4.0 International license](https://creativecommons.org/licenses/by/4.0/). Further distribution of this work must maintain attribution to the author(s) and the published article's title, journal citation, and DOI.

which are sensitively dependent on the configurations of involved 2D monolayers. This tunability is usually achieved through stacking [22], twisting [23], bending [24], or compressing [25] monolayers, which allows for a much higher flexibility and larger potential for tuning novel functionalities than the traditional approach of bulk crystals via covalent chemical bonding.

Although tremendous success has been achieved in vdW stacking of 2D monolayers for building novel structures and systems, the noncovalent interaction prevails only in the stacking direction, while covalent bonding still governs the in-plane position and the types of atoms in each monolayer. Therefore, new strategies have been explored to introduce in-plane noncovalent bonding, namely, using superatomic clusters instead of atoms, as building blocks to construct layered materials. Atomic clusters are also known as superatoms [12,26–30]. These, in principle, have countless species available for materials design [12,29,30]. Here, we do not strictly require the electronic structures of a superatom showing an atomiclike orbital feature [31], such as those in the shells of *S*, *P*, *D*, and others; in other words, we generalize the conventional concept of superatoms. Superatomic crystals could be assembled through various linkage types that usually result in weak intersuperatom electronic interactions [12,26–30]. As an emergent linkage,  $\pi$ - $\pi$  CLQB helps in the formation of free-electron-like bands in pentacene [32] and  $C_{60}$  monolayers [33,34] under finely tuned compression. Nevertheless, electrons in these monolayers were well described in a single-particle picture, with the exception of strong electron-electron or electron-quasiparticle interactions that form the basis of many intriguing and complicated physical phenomena, such as superconductivity [35–37] and charge density waves (CDWs) [37] observed in quantum materials.

Here, we show experimental evidence for the interweaved charge orders in a rationally designed (see Supplemental Material Note 1 [38] for details of the design) layered

material of cubically shaped  $\text{Au}_6\text{Te}_{12}\text{Se}_8$  (ATS) superatomic crystal (Fig. 1), which offers up to 12 Te–Te CLQBs [39,40]. The Te–Te quasibonding in this case is considered a highly interesting noncovalent interaction form because of the reduced energy cost, high tunability, and strong electronic coupling, as illustrated in layered Te allotropes [41,42]. The electronic structures and electrical properties of ATS are revealed using low-temperature scanning-tunneling microscopy (STM) and angle-resolved-photoemission spectroscopy (ARPES) together with Raman and transport measurements, and density-functional theory (DFT) calculations. We find two charge orders, namely, a triple-cube-width stripe period along the *a* axis and a spontaneous electric polarization with interlocked antipolar directions along the *b* axis, which are ascribed to strong electronic interactions. The electronically coupled superatom layers belong to a category of layered materials that exhibit manipulatable novel properties in tremendous layered structures with high and precise tunability (see Fig. S1 in the Supplemental Material [38] for an explanation).

## II. RESULTS

### A. Superatomic crystal and CLQBs

An ATS superatom is composed of orderly arranged Au, Te, and Se atoms in a cubelike highly symmetric geometry, as shown in Fig. 1(a). The three types of atoms are, respectively, located at the faces, edges, and corners of the cubic structure. The lattice of a three-dimensional ATS superatomic crystal may reduce its symmetry, producing *P*2 (*P*211) symmetry on a cleaving surface in the *a*-*b* plane (Supplemental Material Fig. S2 [38]). In this plane, ATS superatom cubes form one-dimensional (1D) chains along the *b* axis, and they slightly slide across chains [Fig. 1(b) and Supplemental Material Fig. S3 [38]]. In contrast to atoms (e.g., Te), the ATS superatoms have a higher interbonding (noncovalent) flexibility, which facilitates the

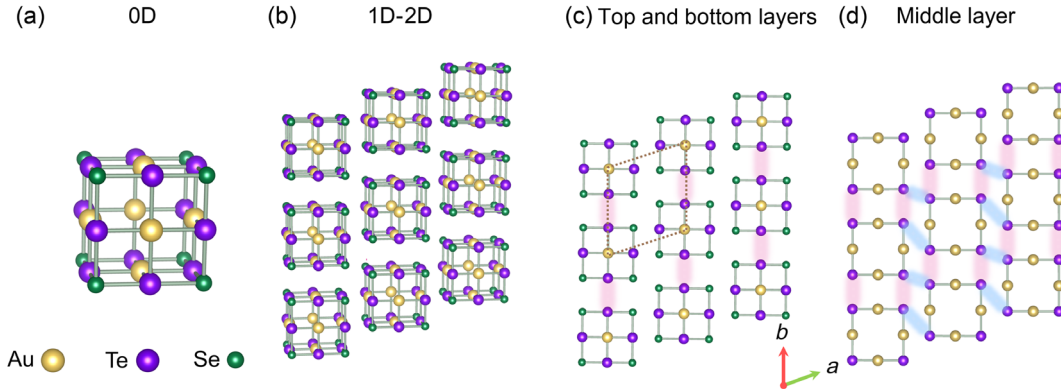


FIG. 1. Atomic structures and intercube interactions of the ATS superatomic crystal. (a) An individual ATS cube structure regarded as a superatom (0D). (b) Atomic structure of an ordered ATS monolayer cleaved from an ATS bulk crystal, in which ATS cubes form 1D chains along the *b* axis. Top views for the slabs of the top and bottom (c) and middle (d) sublayers of the ATS monolayer in which red and blue shadowed lines illustrate intra- (red) and interchain (blue) intercube Te–Te interactions, respectively. Yellow, purple, and green balls represent Au, Te, and Se atoms, respectively.

formation of complicated and highly tunable 2D Te–Te quasibonding networks. In particular, there are four Te–Te noncovalent quasibonds [red shadowed lines in Figs. 1(c) and 1(d)]: one each in the top and bottom sublayers [Fig. 1(c)] and two in the middle sublayer [Fig. 1(d)]. These participate in the formation of ATS chains through noncovalent interactions. Two additional Te–Te bonds [blue shadow lines in Fig. 1(d)] are found only in the middle sublayer, suggesting strong anisotropy of intercube in-plane interactions within the ATS layer surface (Supplemental Material Fig. S4 [38]). Figure S5 in the Supplemental Material [38] shows energy levels and  $|\psi|^2$  of frontier molecular orbitals (MOs) of an isolated ATS cluster. The highest occupied molecular orbital, the lowest unoccupied molecular orbital (LUMO, doublet), and the LUMO + 1 (triplet) are separated from other molecular orbitals by at least 1.0 eV. These three MOs are primarily comprised of pronounced and extended out-of-plane Te-*p*, less significant Se-*p*, and localized in-plane Au-*d* orbitals. The out-of-plane Te-*p* components of these three MOs further result in the strongest Te–Te intercluster interaction for those bands near the Fermi level of the ATS superatomic crystal (Supplemental Material Figs. S6 and S7 [38]), while Te–Se and Te–Au interactions are substantially weaker.

## B. Two sequentially emergent charge orders

Figure 2(a) shows the measured temperature-dependent resistivity and its first-order derivative (differential resistance) for an ATS flake sample. A nearly linear relation is observed for higher temperatures, and the differential resistance begins to drop at approximately 90 K, with the slope becoming much steeper below 80 K. Such a variation in differential resistance suggests the emergence of a likely charge order [43] at 90 K. Further decreasing the sample temperature results in a superconducting transition characteristic appearing at 2.8 K [Figs. 2(a) and Supplemental Material Fig. S8 [38]] [39]. However, the 90-K charge order transition is not reflected in our temperature-dependent Raman shift (TDRS) measurements [Fig. 2(b)], in which three (RP1/3/4) of the five TDRS peaks under our consideration (RP1–5) suggests a transition at approximately 120 K (see Supplemental Material Fig. S9 [38] for more details). Interestingly, the two macroscopic measurements reveal different transition temperatures, stimulating interest in uncovering the origins of this discrepancy.

Figures 2(c)–2(f) show a series of temperature-dependent STM images and their corresponding FFT patterns (in the insets), which are acquired at 80, 100, 120, and 150 K, respectively. The results explicate two charge orders. In particular, the image acquired at 150 K [Fig. 2(f)] exhibits a chainlike appearance, which indicates no charge modulation and confirms the expected anisotropic intercube interactions. A triple-chain-width, stripelike charge modulation appears in the *a* axis at approximately 120 K [Fig. 2(e)] and becomes clearer at approximately 100 K

[Fig. 2(d)]. An additional order emerges along the *b* axis when the temperature decreases to approximately 80 K, which is shown in greater detail in an enlarged STM topographic image acquired at 9 K [Fig. 2(g)]. Surface lattice constants measured via STM ( $a = 9.32$  Å and  $b = 9.08$  Å) are found to be very close to those obtained via DFT calculations ( $a = 9.29$  Å and  $b = 9.04$  Å). The STM image shows multiple chainlike features parallel to the *b* axis. Its FFT pattern confirms the stripe width of three ATS chains, which is in accordance with the observed characteristic peak ( $q^* = a^*/3$ ) on the  $a^*$  axis.

In Fig. 2(i), an enlarged image depicts the additional order of sequentially emergent electrical polarization along the *b* axis (see Supplemental Material Fig. S10 [38]) [44]. In particular, for each stripe period, three chains of the ATS cubes show “up-triangular” (UT), “olive” (*O*), and “down-triangular” (DT) shapes in the occupied state, respectively. Figure 2(j) shows the chain-specific conductance ( $dI/dV$ ) spectra obtained on the UT, *O*, and DT chains. All of these spectra show a quasigap of approximately 0.17 eV around the Fermi level below 120 K (see Supplemental Material Fig. S11 [38]), suggesting their CDW characteristics referred to as triple-cube CDW (TCCDW) hereafter. The formation of TCCDW only in the *a*-axis direction of the ATS crystal does not open a full gap near the Fermi level in each of these spectra, where the density of states (DOS) are incompletely suppressed. These partially suppressed gaps suggest the preserved metallicity of the ATS crystal in the presence of TCCDW, which is confirmed by the transport measurements (see Supplemental Material Note 2 [38] for more details) where an obscure feature is identified only in the secondary differential resistance curve around 100–200 K [Supplemental Material Fig. S8(b) [38]]. Observations of this transition at 120 K using both STM imaging (a surface characterization technique), and Raman and electron-transport measurements (two bulk measurement techniques) indicate that the TCCDW transition occurs both on the surface and in the bulk of the ATS bulk crystal. No apparent temperature-dependent hysteresis is observed in the above experimental measurements (see Supplemental Material Fig. S12 [38] for more details).

## C. Electronic structures of ATS and likely origin of TCCDW

Two types of charge orders sequentially emerge around 90–120 K, namely, the TCCDW order along the *a* axis and an electrical polarization along the *b* axis (Supplemental Material Fig. S13 [38]). Figure 3(a) illustrates the 2D Brillouin zone (BZ) of a cleaved ATS surface, superimposed with its real-space lattice vectors and an atomic model. Figure 3(b) depicts its electronic band structures along highly symmetric directions. Bands 1–4 appear nearly flat along  $\Gamma$ -*X*, whereas they are highly dispersive and cross the Fermi level ( $E_F$ ) along  $\Gamma$ -*Y*. This explicitly indicates the anisotropy of the intercube interactions. These



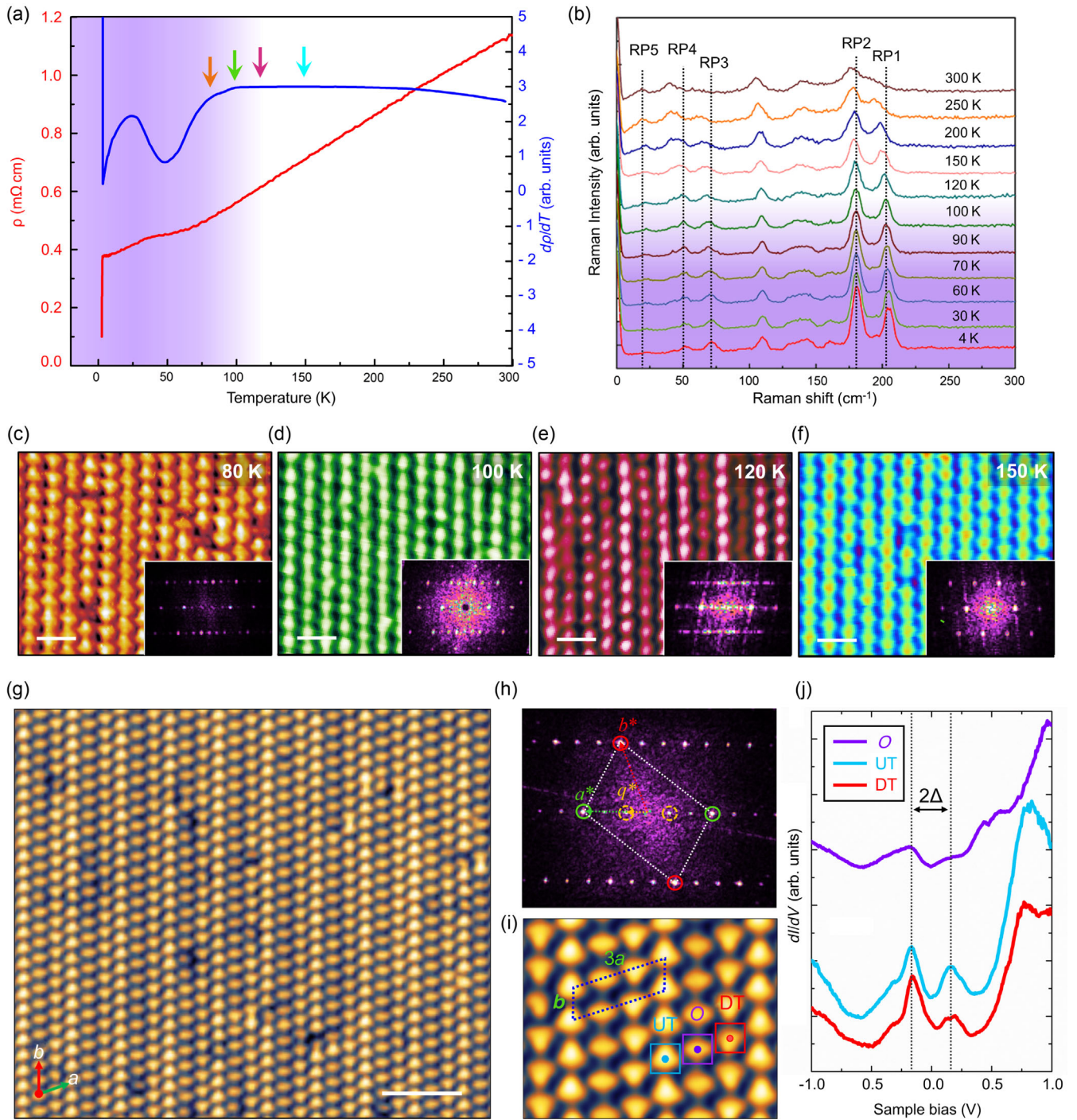


FIG. 2. Charge order transitions in the ATS superatomic crystal. (a) Temperature-dependent resistivity (red) and its derivative (blue) curves. (b) Temperature-dependent Raman spectrum. Five temperature-dependent Raman peaks are marked as RP1–5. (c)–(f) STM topographies and corresponding FFT patterns obtained at 80 K (c), 100 K (d), 120 K (e), and 150 K (f), which are marked by the color-coded arrows in (a). (g) Large-scale STM topography at 9 K. (h) The corresponding FFT of (g). The green and red circles mark the Bravais vectors ( $a^*$  and  $b^*$ ) of the pristine  $a$ - $b$  plane layer, respectively. The orange circles mark the Bravais vectors ( $q^* = a^*/3$ ) of the triple stripe charge order. (i) High-resolution STM image for the  $3 \times 1$  supercell of the triple-cube CDW. (j) STS spectra of the UT, O, and DT cube units showing a charge order gap of approximately 0.17 eV. (g) Scale bar 5 nm,  $V_s = +1.2$  V. (h) Scale bar 2 nm,  $V_s = +1.2$  V.

four bands correspond to the intercubite bonding states along the  $b$  axis, which are hybridized between four pairs of Te atoms on the two facing planes of two adjacent cubes (Supplemental Material Fig. S6 [38]). Band 5 (orange)

intersects bands 3 (light green) and 4 (light pink), which opens two small gaps of 10 meV around points  $1/3$  ( $\Gamma$ -X) and  $2/3$  ( $\Gamma$ -X) in the 2D BZ, respectively, and leaves a flat band nearly sitting at the  $E_F$  between them. Its bandwidth

along  $\Gamma$ -X approaches 0.97 eV but is only 0.50 eV in the  $\Gamma$ -Y direction, indicating stronger across-chain intercube interactions along  $\Gamma$ -X. The anisotropy of intercube interactions in band 5 is confirmed by visualizing its wave-function norm [Supplemental Material Fig. S6(i) [38]] depicting an interchain Te-Te bonding state and nearly isolated ATS cubes within the chain.

These five bands are thus categorized into two groups of highly anisotropic bands according to the plotted band structures and visualized wave-function norms, which are illustrated in the plot of the Fermi surface (FS) shown in Fig. 3(c). The Fermi surface is plotted with a smearing energy of 16 meV. Fermi-surface sheets comprising bands 1–4 are parallel to  $\Gamma$ -X and intersect at different points with a large vertically aligned ellipse originating from band 5. At those intersections, multiple “hot spots” [45] are formed, exhibiting band gaps and embedding a small closed ellipse comprising bands 3–5. The hot spots are connected by vectors that are nearly parallel to the  $\Gamma$ -X direction (red arrows), and their lengths are very close to  $1/3$  ( $\Gamma$ -X). We also calculate the electronic band structure and FS of a monolayer model and present these results in Fig. S7 of the Supplemental Material [38]. It exhibits comparable

electronic structures, that is, bands 1–5 are highly anisotropic and intersect Fermi-surface sheets and ellipse, which indicates weak interlayer electronic coupling in ATS crystals.

The TCCDW may be a result of electron-phonon coupling and/or electron correlation. Our DFT calculations reveal no appreciable atomic displacements accompanied by the TCCDW along the  $a$  axis in both the bulk and monolayer models, indicating the predominant electronic nature of the TCCDW. This electronic nature is also further confirmed by the absence of the Kohn anomaly [46] (see Supplemental Material Fig. S14 [38]) revealed using DFT, nearly identical chain distances observed in our STM imaging (Supplemental Material Fig. S15 [38]), and inappreciable shadow bands induced by band folding in our ARPES spectra (Fig. 3). This implies that electron correlation likely plays a major role in forming the TCCDW. Strong electron-electron interactions between band 5 and bands 1–4, and/or within band 5 are evidenced by the vectors connecting hot-spot pairs, and the large joint density of states (JDOS) originated from the intersecting region. Most corresponding vectors are very close to  $1/3$  ( $\Gamma$ -X). Thus, the observed TCCDW is most likely due to

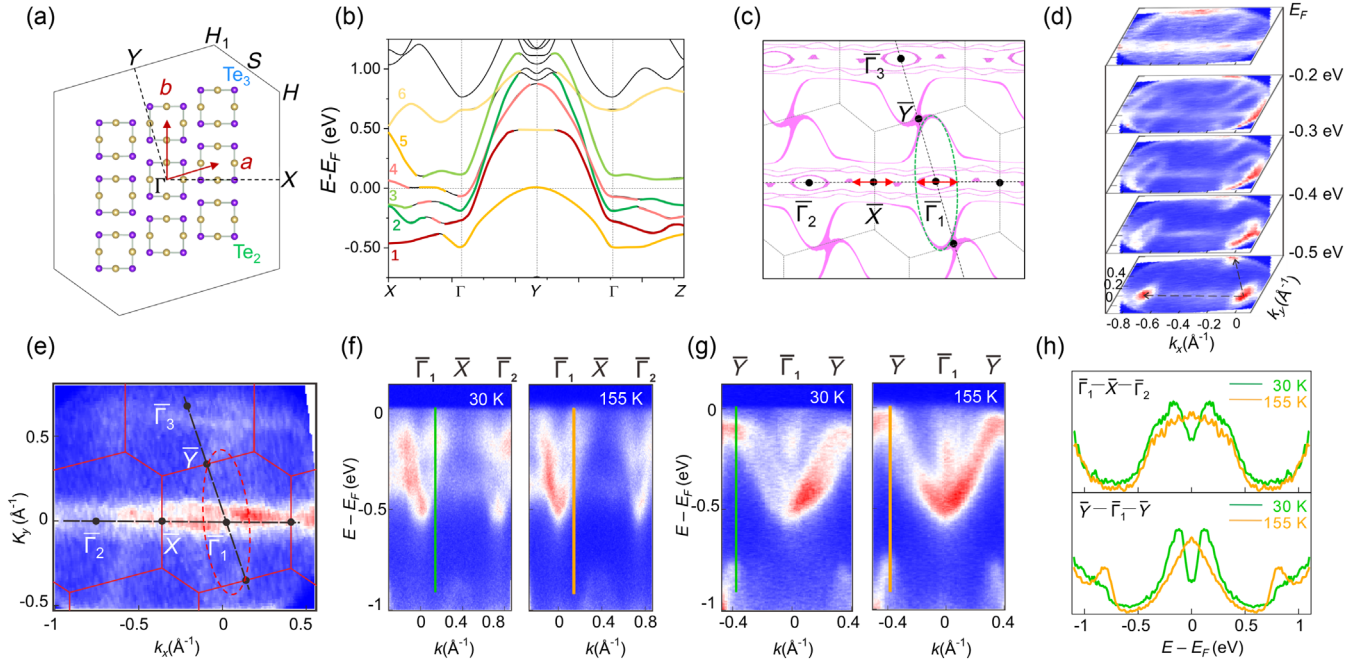


FIG. 3. Electronic structure of the ATS crystal. (a) Two-dimensional BZ of an ATS crystal surface (the  $a$ - $b$  plane) and the corresponding structural model in real space.  $a$  and  $b$  represent the lattice vectors. (b) Theoretical band structure of bulk ATS along highly symmetric lines. Bands 1–6 are numbered according to their orders of eigenenergies at the X point (see Supplemental Material Fig. S6 [38]). (c) Constant-energy contours in the 2D Brillouin zone ( $k_z = 0$ ) at the adjacent Fermi level with an energy broadening of  $\pm 8$  meV. The red arrows indicate two typical nesting vectors relevant with the TCCDW. (d) Constant-energy intensity plots with respect to the Fermi level obtained from ARPES measurements. Two high-symmetry paths ( $\Gamma$ -X- $\Gamma$  and  $\Gamma$ -Y- $\Gamma$ ) are indicated using two black dashed lines at the  $-0.5$  eV plane. (e) Integrated intensity plot with  $E_F \pm 40$  meV. The large elliptical FS is marked using a red dashed line. (f, g) Two-dimensional intensity plots measured along  $\Gamma_1$ -X- $\Gamma_2$  (f) and Y- $\Gamma_1$ -Y (g) at  $T = 30$  K (left) and  $T = 155$  K (right), respectively. (h) The symmetrized energy distribution curves at  $1/3$  ( $\Gamma$ -X) and the Y point from (f) and (g), as measured at 30 K (green) and 155 K (orange), respectively.



strong interchain Coulomb interaction across ATS chains through Te–Te quasibonding in the middle sublayer and significant electron hopping along ATS chains (the  $b$  axis) through Te–Te noncovalent interactions in all sublayers. In addition, those two categories of anisotropic bands (i.e., bands 1–4 versus band 5) indicate stronger intercubane interactions within the chains (along the  $b$  axis). Therefore, each chain on the surface can be qualitatively regarded as one supersite, and the surface can thus be modeled in a 1D FS nesting picture [47–49] along the  $a$  axis (Supplemental Material Fig. S16 [38]), explaining the tendency to form a quasi-1D CDW along that direction.

While our DFT results indicate that both strong Coulomb interactions and significant electron hopping can be utilized through noncovalent interactions in the ATS layer, the predicted electronic structures are experimentally verified using ARPES measurements. Figure 3(d) shows constant-energy plots starting at  $E_F$  and decreasing by 0.5 eV below  $E_F$  at  $T = 30$  K. The figure shows two converged points in the intensity map acquired at  $-0.5$  eV, which correspond to the  $\Gamma_1$  and  $\Gamma_2$  points of two adjacent BZs, respectively. Determination of the  $\Gamma$  point position allows for the further derivation of the positions of high symmetry lines  $\Gamma$ – $Y$  and  $\Gamma$ – $X$  and the BZ boundary. Figure 3(e) shows the intensity map at  $E_F$ , in which the 2D BZ boundary is highlighted in red solid lines. The large elliptical Fermi surface (indicated by the red dashed lines) and the relatively flat Fermi sheets along  $\Gamma$ – $X$  are clearly resolved, which is highly consistent with the calculated FS shown in Fig. 3(c).

Band dispersion measurements are performed at  $T = 30$  and 155 K, to clarify the origin of the partial gap found in scanning-tunneling spectroscopy (STS). Two cuts along high-symmetry lines  $\Gamma_1$ – $X$ – $\Gamma_2$  and  $Y$ – $\Gamma_1$ – $Y$  are presented in Figs. 3(f) and 3(g), respectively. Along  $\Gamma_1$ – $X$ – $\Gamma_2$ , a dispersive band (band 5) crosses the  $E_F$  near  $1/3$  ( $\Gamma$ – $X$ ) at 155 K, and an electronic band gap is opened around  $E_F$  at 30 K. Along  $Y$ – $\Gamma_1$ – $Y$ , band 5 reaches the Fermi level near the  $Y$  point at 155 K, but it opens a band gap around  $E_F$  at 30 K. The gaps along the two lines are more clearly revealed using symmetrized energy-distribution-curve cuts, as shown in Fig. 3(h). The determined gap size is 135 meV (at 30 K) comparable with the STS result of approximately 0.17 eV (at 9 K).

#### D. Interweaving polar electronic states

Electrical polarization along the  $b$  axis is clearly resolved in STM imaging, which breaks the degeneracy of intercubane Te–Te interactions within ATS chains that reduces the JDOS near the  $Y$  point [Figs. 3(b) and 3(c)]. Figures 4(a) and 4(b) show high-resolution STM images of the filled and empty states of the (UT– $O$ –DT) tricube, respectively. Remarkably, the directions of each triangular chain (UT and DT) are oriented opposite each other in the filled- and empty-state images. This indicates that the polarization along the  $b$  axis is relevant with electronic hybridization, whereas

no polarization occurs in the cubes of  $O$  chains. Figures 4(c)–4(e) provide an illustration showing the formed electrical dipoles, which are ascribed to charge polarization within the UT and DT cubes along the  $b$  axis. The dipoles are parallelly aligned within the UT and DT chains but anti-parallelly oriented between UT and DT chains (see Supplemental Material Fig. S17 [38]).

Appreciable accumulation of (depleted) DOS is found at the UT– $O$  and  $O$ –DT interchain regions in the filled-state (empty-state) image [Figs. 4(a) and 4(b)] pointing toward the essential roles that the interchain electronic hybridization plays in inducing these polarized electronic states. Figure 4(f) depicts interchain differential charge density (DCD) in the middle (left panel) and top and bottom (right panel) sublayers of an ATS monolayer in the triple-cube stripe configuration. The middle sublayer engenders strong interchain interactions where covalentlike Te–Te hybridizations, that is, charge reduction (blue) near Te atoms and charge accumulation (red) in between them, are identified in the interchain region. On the top and bottom sublayers, we observe enhanced interchain Te–Se covalentlike characteristics and slightly weakened intrachain Te–Te interactions, as reflected by charge accumulation in the interchain areas and charge reduction at the intercubane region within chains, respectively.

Electronic interactions, primarily hybridization, are capable of introducing spatially polarized distribution of electronic states along the  $b$  axis in the UT and DT chains, which are clearly evidenced by the projected DOS (PDOS) of Te atoms at the top sublayer [Figs. 4(g)–4(i) and Supplemental Material Fig. S13 [38]]. Compared to the  $\text{Te}_{T1}$  atom from the nonpolarized  $O$  chain, atoms  $\text{Te}_{T2}$  and  $\text{Te}_{T3}$  of the UT and DT chains display apparent inversion-symmetry breaking. Representative peaks  $P_{T2}$  and  $P_{T3}$  separated by 35 meV are both distributed on  $\text{Te}_{T1}$  and preferably located on  $\text{Te}_{T2}$  and  $\text{Te}_{T3}$ , respectively, showing significant electrical polarization in the UT and DT chains. Real-space wave-function norms of these two peaks are visualized in Figs. 4(h) and 4(i), which display strongly polarized states (inversion-symmetry breaking) along the  $b$  axis in the UT and DT chains and inversion-symmetric states for the  $O$  chain.

### III. DISCUSSION

As discussed in detail elsewhere [50], the TCCDW (along the  $a$  axis) coexists with the emergent superconductivity (below approximately 3 K) under ambient pressure, but they compete under high pressures. This TCCDW also essentially enhances the UT– $O$  and  $O$ –DT across-chain interactions, which strengthens Te–Te electronic hybridizations in the across-chain direction but leaves the inversion symmetry maintained for the  $O$ -chain cubes. This reinforced hybridization tends to reduce the high JDOS near the  $Y$  point and to lift the degeneracy of intercubane electronic states within chains. Consequently, polarized

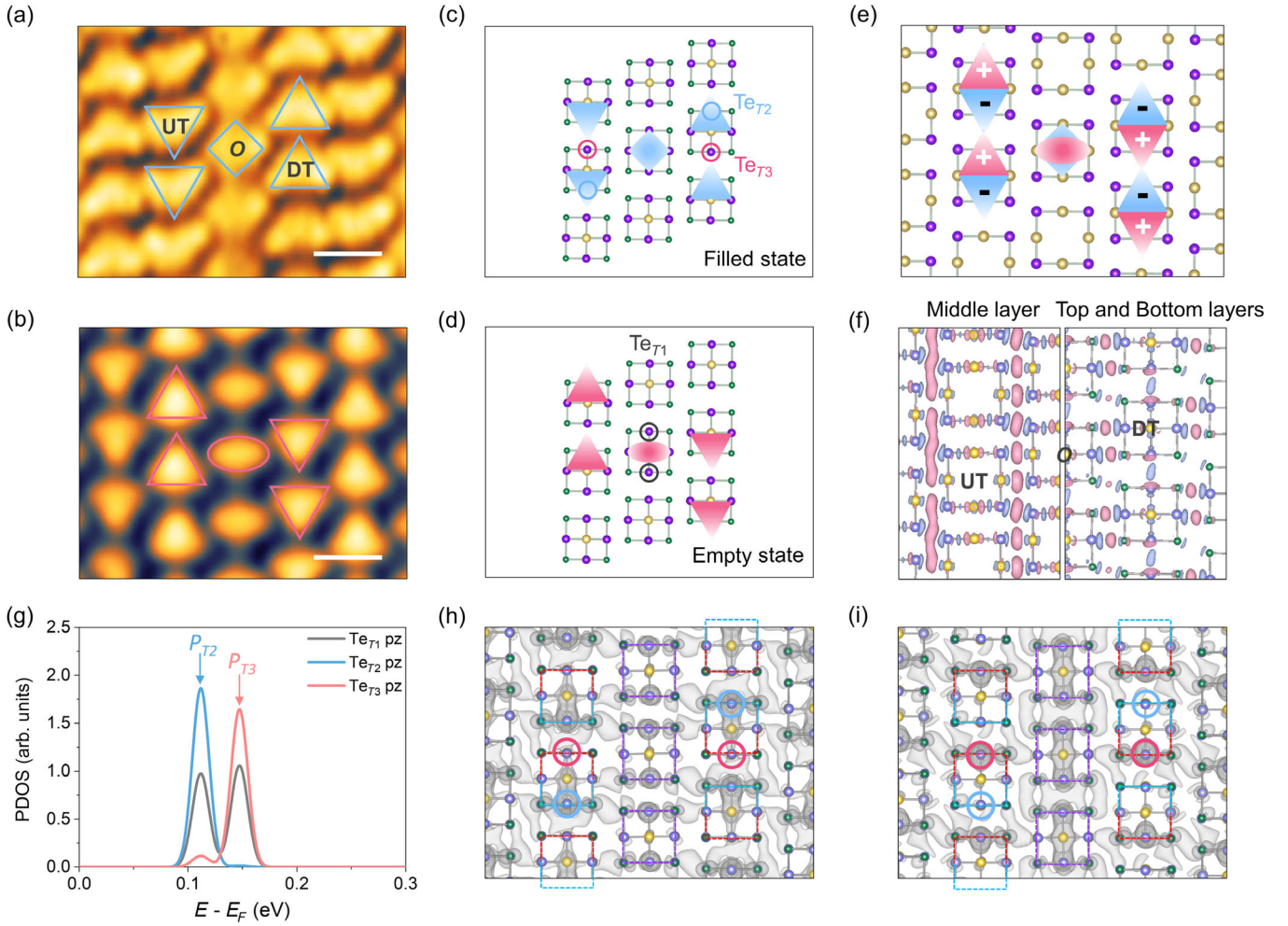


FIG. 4. Antipolar electronic states of ATS cubes. (a),(b) STM topographic images of the ATS cubes at filled (a) and empty states (b), respectively. (a) Scale bar 1 nm,  $V_s = +1.2$  V. (b) Scale bar 1 nm,  $V_s = -1.2$  V. They show interchain bondinglike (c) and antibondinglike (d) states among the (UT-O-DT) tricube. (e) Illustration of polarized electronic states in filled and empty states. (f) Interchain DCD of an ATS monolayer where red and blue contours represent charge accumulation and depletion, respectively. Slabs of middle and top and bottom are shown in the left and right panels, respectively. The isosurface value is  $0.0005 e/\text{bohr}^3$ . (g) PDOS of  $p_z$  orbitals of three types of Te atoms, as denoted in (c) and (d), in the top sublayer. (h),(i) Wave-function norms of states  $P_{T2}$  (h) and  $P_{T3}$  (i), respectively, where the dashed boxes outline ATS cubes.

electronic states (along the  $b$  axis) are formed at low temperature. An antiparallel polarized configuration is thus locked to maintain the inversion symmetry of the  $O$  cube. In other words, specific antipolarization configurations are selectively determined by the TCCDW charge order, which explains the use of the term “interweaving polar charge” orders.

Spatially polarized metallic states were originally proposed by Anderson and Blount in 1965 [51]. Until now, roughly 40 types of polar metallic materials have been theoretically predicted [52]; however, only a few of these have been discovered and experimentally confirmed [53–55]. Nevertheless, an antipolar metallic state is discovered in this study, in which the antipolar state is primarily uncovered using STM imaging in the real space, while the metallic state is verified in both cube-resolved STS and

macroscopic electrical-transport measurements. The antipolar metallic state is primarily ascribed to strong electronic interactions rather than spatial displacements of atoms.

In summary, we demonstrate that strong electron-electron interactions are at play in a noncovalently bonded layered superatomic crystal. Such exceptionally strong interaction leads to the TCCDW, the spatially polarized electronic states, and their interweaving antipolar configuration coexisting with metallic states. These findings reveal that superatomic crystals comprising atomic clusters through noncovalent interactions are suitable for the exploration, manipulation, and utilization of exotic electronic properties, which were traditionally investigated in covalently bonded solids. Given the high tunability of superatoms, more superatomic solids and layers can be proposed, prepared, or even rationally designed by tailoring

their superatomic building blocks and the interblock interactions among them. This allows for the exploration of those parameter regimes and thus the observation of emergent phenomena that were inaccessible in conventional quantum materials.

#### IV. MATERIALS AND METHODS

##### A. Sample preparation and STM measurements

Single crystals of ATS are grown by the self-flux method. They are in the shape of small platelets with shining mirrorlike surfaces, typically  $2 \times 4 \times 1 \text{ mm}^3$ . Samples are cleaved in ultrahigh vacuum at room temperature and subsequently cooled for STM measurements, which are performed in a commercial variable-temperature STM (PanScan Freedom, RHK) operated in ultrahigh vacuum. Electrochemically etched polycrystalline tungsten calibrated on clean Au(111) surfaces is used for all our STM measurements tips. The STM topography is acquired in the constant-current mode, and the  $dI/dV$  spectra are collected using a standard lock-in technique with a modulation frequency of 999.1 Hz. STM measurements are performed mostly at 9 K for high-resolution imaging, and at variable temperatures (from 9 K to room temperature) for the phase transition characterization.

##### B. XRD, SEM, and transport measurements

Powder x-ray-diffraction patterns of polycrystalline ATS are measured using a PANalytical X'Pert diffractometer with the Cu- $K_\alpha$  anode ( $\lambda = 1.5408 \text{ \AA}$ ). Scanning-electron-microscopy (SEM) images of the ATS single crystal are acquired using a Hitachi S-4800 FE-SEM. Electrical resistivity ( $\rho$ ) is measured using the standard four-wire method in a physical property measurement system (Quantum Design).

##### C. Raman measurements

Raman spectroscopy measurements are performed using a home-built low-wave-number and variable-temperature Raman system equipped with a semiconductor laser ( $\lambda = 532 \text{ nm}$ ),  $50\times$  objective (numerical aperture 0.8), and a  $600\text{-line-mm}^{-1}$  grating. The sample is placed in a cryostat (attocube800 systems AG, Germany). To prevent potential CDW phase transitions induced by laser irradiation, the laser irradiance is kept below  $100 \mu\text{W}/\mu\text{m}^2$ . Low-wave-number Raman filters (Ondax Inc., USA) are used to achieve a cutoff Raman shift down to approximately  $10 \text{ cm}^{-1}$ . The step size of the Raman mapping is  $1 \mu\text{m}$ . All the peaks are calibrated with the Si peak at  $520.7 \text{ cm}^{-1}$ .

##### D. ARPES measurements

ARPES measurements are performed at Renmin University of China using a Scienta DA30 analyzer and at

a photon energy of  $10.05 \text{ eV}$ , as well as at the BL13U beamline of the National Synchrotron Radiation Laboratory equipped with a Scienta R4000 analyzer. The energy and angular resolution are set to  $10 \text{ meV}$  and  $0.3^\circ$ , respectively. Clean surfaces for ARPES measurements are obtained by *in situ* sample cleaving. Photoemission spectra presented in this study are recorded at  $T = 30$  and  $155 \text{ K}$  using photon energy from 21 to  $45 \text{ eV}$  in a working ultrahigh vacuum better than  $6 \times 10^{-11} \text{ Torr}$ .

##### E. Theoretical calculations

Density-functional theory calculations are performed using the generalized-gradient approximation for the exchange-correlation potential, the projector-augmented-wave method [56,57], and a plane-wave basis set as implemented in the Vienna *ab initio* simulation package (VASP) [58] and QUANTUM ESPRESSO package [59]. Dispersion corrections are made at the van der Waals density-functional (vdW-DF) level [60,61], with the optB86b functional for the exchange potential (optB86b-vdW) [62,63]. The kinetic energy cutoff for the plane-wave basis is set to 700 and 350 eV for all geometric property and electronic structure calculations, respectively. Two  $k$  meshes of  $7 \times 7 \times 5$  and  $7 \times 7 \times 1$  are used to sample the first Brillouin zone in structure optimizations of the bulk and monolayer ATS crystals, respectively. The  $k$  meshes are increased to  $15 \times 15 \times 15$  and  $15 \times 15 \times 1$  in electronic structure calculations. An even denser  $k$  mesh of  $30 \times 30 \times 1$  is used to plot the 2D Fermi surface of the bulk ( $k_z = 0$ ) and monolayer crystals. Density-functional-perturbation theory [64] is employed to calculate the vibrational frequencies of the ATS bulk crystal at the  $\Gamma$  point and point  $q_{\text{TCCDW}} = (1/3, 0, 0)$  in the reciprocal space using the VASP and QUANTUM ESPRESSO packages, respectively. A  $3 \times 1$  supercell is used to model the ATS monolayer in the TCCDW state. The Brillouin zone is sampled using a  $2 \times 7 \times 1$   $k$  mesh for both structural optimizations and electronic structure calculations. A vacuum layer of  $17 \text{ \AA}$  is used to eliminate image interactions among adjacent supercells. The shape and volume of the supercell and all atomic positions are fully relaxed until the residual force per atom is less than  $0.01 \text{ eV/\AA}$ . A Methfessel-Paxton smearing of  $0.05 \text{ eV}$  and the Bloch-corrected-tetrahedron method are used for the Brillouin-zone integral in calculations of the geometric and electronic structures, respectively. A Gaussian smearing of  $0.01 \text{ eV}$  is used to plot the projected density of states for the  $3 \times 1$  supercell. We calculate charge densities of three single ATS chains (i.e.,  $\rho_{\text{UT}}$ ,  $\rho_{\text{O}}$ , and  $\rho_{\text{DT}}$ ) using the same geometry and precision as those in the  $3 \times 1$  supercell and subtract them from the total charge density of the supercell ( $\rho_{\text{total}}$ ), thereby obtaining the interchain differential charge density ( $\rho_{\text{DCD}}$ ), i.e.,  $\rho_{\text{DCD}} = \rho_{\text{total}} - \rho_{\text{UT}} - \rho_{\text{O}} - \rho_{\text{DT}}$ .



## ACKNOWLEDGMENTS

This project is supported by the Strategic Priority Research Program (Chinese Academy of Sciences) (Grant No. XDB30000000), the Ministry of Science and Technology of China (Grants No. 2018YFE0202700 and No. 2016YFA0200700), the National Natural Science Foundation of China (Grants No. 61674045, No. 11604063, No. 61911540074, No. 51922105, No. 11774421, No. 61761166009, and No. 11974422), and the Fundamental Research Funds for the Central Universities and the Research Funds of Renmin University of China under Grants No. 21XNLG27 (Z. C.) and No. 22XNKJ30 (W. J.). L. W. is supported by the Outstanding Innovative Talents Cultivation Funded Programs 2022 of Renmin University of China. Calculations are performed at the Physics Lab of High-Performance Computing of Renmin University of China, Shanghai Supercomputer Center.

S. X., L. W., Z. W., and X. C. contributed equally to this work. Z. C., S. W., J. G., and W. J. conceived the research project. S. X., L. L., Q. Z., X. L., L. H., H. J. G., and Z. C. performed the STM experiments and analysis of STM data. Z. W. and S. W. performed the ARPES experiments and analysis of ARPES data. X. C., J. G., and X. C. grew the single crystals and performed transport, SEM, and XRD measurements. H. L., S. H., S. C., and L. X. performed Raman measurements. L. W., L. Z., and W. J. performed the DFT calculations. S. X., L. W., Z. W., Z. C., S. W., and W. J. wrote the manuscript with input from all authors.

- [1] Y. Kamihara, T. Watanabe, M. Hirano, and H. Hosono, *Iron-Based Layered Superconductor*  $\text{LaO}_{1-x}\text{F}_x\text{FeAs}$  ( $x = 0.05\text{--}0.12$ ) with  $T_c = 26$  K, *J. Am. Chem. Soc.* **130**, 3296 (2008).
- [2] Y. Liu, P. Trimby, L. Collins, M. Ahmadi, A. Winkelmann, R. Proksch, and O. S. Ovchinnikova, *Correlating Crystallographic Orientation and Ferroic Properties of Twin Domains in Metal Halide Perovskites*, *ACS Nano* **15**, 7139 (2021).
- [3] L. Etgar, P. Gao, Z. Xue, Q. Peng, A. K. Chandiran, B. Liu, M. K. Nazeeruddin, and M. Graetzel, *Mesoscopic  $\text{CH}_3\text{NH}_3\text{PbI}_3/\text{TiO}_2$  Heterojunction Solar Cells*, *J. Am. Chem. Soc.* **134**, 17396 (2012).
- [4] H. Huang, J. Raith, S. V. Kershaw, S. Kalytchuk, O. Tomanec, L. Jing, A. S. Susha, R. Zboril, and A. L. Rogach, *Growth Mechanism of Strongly Emitting  $\text{CH}_3\text{NH}_3\text{PbBr}_3$  Perovskite Nanocrystals with a Tunable Bandgap*, *Nat. Commun.* **8**, 996 (2017).
- [5] L. L. a. G. and N. W. Handy, *A Study of the Chromous-Chromic Iodide Equilibrium*, *J. Am. Chem. Soc.* **72**, 5049 (1950).
- [6] B. Huang, G. Clark, E. Navarro-Moratalla, D. R. Klein, R. Cheng, K. L. Seyler, D. Zhong, E. Schmidgall, M. A. McGuire, D. H. Cobden *et al.*, *Layer-Dependent Ferromagnetism in a van der Waals Crystal down to the Monolayer Limit*, *Nature (London)* **546**, 270 (2017).
- [7] P. Li, C. Wang, J. Zhang, S. Chen, D. Guo, W. Ji, and D. Zhong, *Single-Layer  $\text{CrI}_3$  Grown by Molecular Beam Epitaxy*, *Sci. Bull.* **65**, 1064 (2020).
- [8] Q. Gu, Y. Li, S. Wan, H. Li, W. Guo, H. Yang, Q. Li, X. Zhu, X. Pan, Y. Nie *et al.*, *Single Particle Tunneling Spectrum of Superconducting  $\text{Nd}_{1-x}\text{Sr}_x\text{NiO}_2$  Thin Films*, *Nat. Commun.* **11**, 6027 (2020).
- [9] S. Jia, P. Jiramongkolchai, M. R. Suchomel, B. H. Toby, J. G. Checkelsky, N. P. Ong, and R. J. Cava, *Ferromagnetic Quantum Critical Point Induced by Dimer-Breaking in  $\text{SrCo}_2(\text{Ge}_{1-x}\text{P}_x)_2$* , *Nat. Phys.* **7**, 207 (2011).
- [10] D. Hirai, F. von Rohr, and R. J. Cava, *Emergence of Superconductivity in  $\text{BaNi}_2(\text{Ge}_{1-x}\text{P}_x)_2$  at a Structural Instability*, *Phys. Rev. B* **86**, 100505(R) (2012).
- [11] K. L. Reifsnider, R. Raihan, and Q. Liu, *Rational Durability Design of Heterogeneous Functional Materials: Some First Principles*, *Mechanics of Composite Materials* **49**, 21 (2013).
- [12] E. A. Doud, A. Voevodin, T. J. Hochuli, A. M. Champsaur, C. Nuckolls, and X. Roy, *Superatoms in Materials Science*, *Nat. Rev. Mater.* **5**, 371 (2020).
- [13] Y. Zhao, J. Qiao, P. Yu, Z. Hu, Z. Lin, S. P. Lau, Z. Liu, W. Ji, and Y. Chai, *Extraordinarily Strong Interlayer Interaction in 2D Layered  $\text{PtS}_2$* , *Adv. Mater.* **28**, 23999 (2016).
- [14] J. Qiao, Y. Pan, F. Yang, C. Wang, Y. Chai, and W. Ji, *Few-Layer Tellurium: One-Dimensional-like Layered Elementary Semiconductor with Striking Physical Properties*, *Science bulletin* **63**, 159 (2018).
- [15] Y. Zhao, J. Qiao, Z. Yu, P. Yu, K. Xu, S. P. Lau, W. Zhou, Z. Liu, X. Wang, W. Ji *et al.*, *High-Electron-Mobility and Air-Stable 2D Layered  $\text{PtSe}_2$  FETs*, *Adv. Mater.* **29**, 1604230 (2017).
- [16] J. Qiao, X. Kong, Z. X. Hu, F. Yang, and W. Ji, *High-Mobility Transport Anisotropy and Linear Dichroism in Few-Layer Black Phosphorus*, *Nat. Commun.* **5**, 4475 (2014).
- [17] P. J. Guo, X. Q. Lu, W. Ji, K. Liu, and Z. Y. Lu, *Quantum Spin Hall Effect in Monolayer and Bilayer  $\text{TaIrTe}_4$* , *Phys. Rev. B* **102**, 041109(R) (2020).
- [18] P. Jiang, C. Wang, D. Chen, Z. Zhong, Z. Yuan, Z. Y. Lu, and W. Ji, *Stacking Tunable Interlayer Magnetism in Bilayer  $\text{CrI}_3$* , *Phys. Rev. B* **99**, 144401 (2019).
- [19] N. Sivasdas, S. Okamoto, X. Xu, C. J. Fennie, and D. Xiao, *Stacking-Dependent Magnetism in Bilayer  $\text{CrI}_3$* , *Nano Lett.* **18**, 7658 (2018).
- [20] Y. Gao, M. Wu, and P. Jena, *A Family of Ionic Supersalts with Covalent-like Directionality and Unconventional Multiferroicity*, *Nat. Commun.* **12**, 1331 (2021).
- [21] J. Guo, Y. Qi, S. Matsuishi, and H. Hosono,  *$T_c$  Maximum in Solid Solution of Pyrite  $\text{IrSe}_2\text{--RhSe}_2$  Induced by Destabilization of Anion Dimers*, *J. Am. Chem. Soc.* **134**, 20001 (2012).
- [22] A. K. Geim and I. V. Grigorieva, *van der Waals Heterostructures*, *Nature (London)* **499**, 419 (2013).
- [23] Y. Cheng, C. Huang, H. Hong, Z. Zhao, and K. Liu, *Emerging Properties of Two-Dimensional Twisted Bilayer Materials*, *Chin. Phys. B* **28**, 107304 (2019).

- [24] R. I. Gonzalez, F. J. Valencia, J. Rogan, J. A. Valdivia, J. Sofo, M. Kiwi, and F. Munoz, *Bending Energy of 2D Materials: Graphene, MoS<sub>2</sub> and Imogolite*, *RSC Adv.* **8**, 4577 (2018).
- [25] A. F. Kusmartseva, B. Sipos, H. Berger, L. Forro, and E. Tutis, *Pressure Induced Superconductivity in Pristine 1T-TiSe<sub>2</sub>*, *Phys. Rev. Lett.* **103**, 236401 (2009).
- [26] W. Han, P. Huang, L. Li, F. Wang, P. Luo, K. Liu, X. Zhou, H. Li, X. Zhang, Y. Cui *et al.*, *Two-Dimensional Inorganic Molecular Crystals*, *Nat. Commun.* **10**, 4728 (2019).
- [27] A. Voevodin, L. M. Campos, and X. Roy, *Multifunctional Vesicles from a Self-Assembled Cluster-Containing Diblock Copolymer*, *J. Am. Chem. Soc.* **140**, 5607 (2018).
- [28] P. Jena and A. W. Castleman, Jr., *Clusters: A Bridge across the Disciplines of Physics and Chemistry*, *Proc. Natl. Acad. Sci. U.S.A.* **103**, 10560 (2006).
- [29] P. Jena and Q. Sun, *Super Atomic Clusters: Design Rules and Potential for Building Blocks of Materials*, *Chem. Rev.* **118**, 5755 (2018).
- [30] P. Jena and Q. Sun, *Theory-Guided Discovery of Novel Materials*, *J. Phys. Chem. Lett.* **12**, 6499 (2021).
- [31] M. Feng, J. Zhao, and H. Petek, *Atomlike, Hollow-Core-Bound Molecular Orbitals of C<sub>60</sub>*, *Science* **320**, 359 (2008).
- [32] A. Maliakal, K. Raghavachari, H. Katz, E. Chandross, and T. Siegrist, *Photochemical Stability of Pentacene and a Substituted Pentacene in Solution and in Thin Films*, *Chem. Mater.* **16**, 4980 (2004).
- [33] X. Cui, D. Han, H. Guo, L. Zhou, J. Qiao, Q. Liu, Z. Cui, Y. Li, C. Lin, L. Cao *et al.*, *Realizing Nearly-Free-Electron Like Conduction Band in a Molecular Film through Mediating Intermolecular van der Waals Interactions*, *Nat. Commun.* **10**, 3374 (2019).
- [34] G. Li, H. T. Zhou, L. D. Pan, Y. Zhang, J. H. Mao, Q. Zou, H. M. Guo, Y. L. Wang, S. X. Du, and H. J. Gao, *Self-Assembly of C<sub>60</sub> Monolayer on Epitaxially Grown, Nanostructured Graphene on Ru(0001) Surface*, *Appl. Phys. Lett.* **100**, 013304 (2012).
- [35] P. W. Anderson, *The Resonating Valence Bond State in La<sub>2</sub>CuO<sub>4</sub> and Superconductivity*, *Science* **235**, 1196 (1987).
- [36] J. Guo, S. Jin, G. Wang, S. Wang, K. Zhu, T. Zhou, M. He, and X. Chen, *Superconductivity in the Iron Selenide K<sub>x</sub>Fe<sub>2</sub>Se<sub>2</sub> (0 ≤ x ≤ 1.0)*, *Phys. Rev. B* **82**, 180520(R) (2010).
- [37] R. Ang, Y. Tanaka, E. Ieki, K. Nakayama, T. Sato, L. J. Li, W. J. Lu, Y. P. Sun, and T. Takahashi, *Real-Space Coexistence of the Melted Mott State and Superconductivity in Fe-Substituted 1T-TaS<sub>2</sub>*, *Phys. Rev. Lett.* **109**, 176403 (2012).
- [38] See Supplemental Material at <http://link.aps.org/supplemental/10.1103/PhysRevX.12.041034> for the discussions of the “design process,” the XRD and SEM characterizations, the bias dependent and area dependent STM topographic images, the temperature-dependent transport and Raman measurements and the theoretical vibrational frequencies of the ATS bulk crystal, the electronic structures of the ATS single cube, monolayer and bulk crystal, and the discussion and schematics of the mechanisms of the TCCDW and the antipolar metal.
- [39] J. G. Guo, X. Chen, X. Y. Jia, Q. H. Zhang, N. Liu, H. C. Lei, S. Y. Li, L. Gu, S. F. Jin, and X. L. Chen, *Quasi-Two-Dimensional Superconductivity from Dimerization of Atomically Ordered AuTe<sub>2</sub>Se<sub>4/3</sub> Cubes*, *Nat. Commun.* **8**, 871 (2017).
- [40] X. Y. Jia, Y. J. Yu, X. Chen, J. G. Guo, T. P. Ying, L. P. He, X. L. Chen, and S. Y. Li, *Nodeless Superconductivity in a Quasi-Two-Dimensional Superconductor AuTe<sub>2</sub>Se<sub>4/3</sub>*, *Chin. Phys. B* **27**, 067401 (2018).
- [41] A. Fang, N. Ru, I. R. Fisher, and A. Kapitulnik, *STM Studies of TbTe<sub>3</sub>: Evidence for a Fully Incommensurate Charge Density Wave*, *Phys. Rev. Lett.* **99**, 046401 (2007).
- [42] C. Malliakas, S. J. L. Billinge, H. J. Kim, and M. G. Kanatzidis, *Square Nets of Tellurium: Rare-Earth Dependent Variation in the Charge-Density Wave of RETe<sub>3</sub> (RE = Rare-Earth Element)*, *J. Am. Chem. Soc.* **127**, 6510 (2005).
- [43] S. J. Denholme, A. Yukawa, K. Tsumura, M. Nagao, R. Tamura, S. Watauchi, I. Tanaka, H. Takayanagi, and N. Miyakawa, *Coexistence of Superconductivity and Charge-Density Wave in the Quasi-One-Dimensional Material HfTe<sub>3</sub>*, *Sci. Rep.* **7**, 45217 (2017).
- [44] M. Spera, A. Scarfato, Á. Pásztor, E. Giannini, D. R. Bowler, and Ch. Renner, *Insight into the Charge Density Wave Gap from Contrast Inversion in Topographic STM Image*, *Phys. Rev. Lett.* **125**, 267603 (2020).
- [45] Y. Yamakawa and H. Kontani, *Spin-Fluctuation-Driven Nematic Charge-Density Wave in Cuprate Superconductors: Impact of Aslamazov-Larkin Vertex Corrections*, *Phys. Rev. Lett.* **114**, 257001 (2015).
- [46] W. Kohn, *Image of the Fermi Surface in the Vibration Spectrum of a Metal*, *Phys. Rev. Lett.* **2**, 393 (1959).
- [47] X. Zhu, J. Guo, J. Zhang, and E. W. Plummer, *Misconceptions Associated with the Origin of Charge Density Waves*, *Adv. Phys.* **2**, 622 (2017).
- [48] G. Gruner, *Density Waves in Solids* (Addison-Wesley Publishing Company, Reading, MA, 1994), Vol. 89.
- [49] R. E. Peierls, *Quantum Theory of Solids* (Oxford University Press, London, 1955), pp. 433–435.
- [50] X. Chen, G. Fei, Y. Song, T. Ying, D. Huang, B. Pan, X. Yang, K. Chen, X. Zhan, J. Wang *et al.*, *Superatomic-Charge-Density-Wave in Cluster-Assembled AuTe<sub>2</sub>Se<sub>4/3</sub> Superconductors*, *J. Am. Chem. Soc.* **144**, 20915 (2022).
- [51] P. W. B. Anderson and E. I. Blount, *Symmetry Considerations on Martensitic Transformations: “Ferroelectric” Metals?*, *Phys. Rev. Lett.* **14**, 532 (1965).
- [52] W. X. Zhou and A. Ariando, *Review on Ferroelectric/polar Metals*, *Jpn. J. Appl. Phys.* **59**, SI0802 (2020).
- [53] Z. Fei, W. Zhao, T. A. Palomaki, B. Sun, M. K. Miller, Z. Zhao, J. Yan, X. Xu, and D. H. Cobden, *Ferroelectric Switching of a Two-Dimensional Metal*, *Nature (London)* **560**, 336 (2018).
- [54] P. Sharma, F. X. Xiang, D. F. Shao, D. Zhang, E. Y. Tsymbal, A. R. Hamilton, and J. Seidel, *A Room-Temperature Ferroelectric Semimetal*, *Sci. Adv.* **5**, eaax5080 (2019).
- [55] T. H. Kim, D. Puggioni, Y. Yuan, L. Xie, H. Zhou, N. Campbell, P. J. Ryan, Y. Choi, J. W. Kim, J. R. Patzner *et al.*, *Polar Metals by Geometric Design*, *Nature (London)* **533**, 68 (2016).
- [56] P. E. Blochl, *Projector Augmented-Wave Method*, *Phys. Rev. B* **50**, 17953 (1994).

- [57] G. Kresse and D. Joubert, *From Ultrasoft Pseudopotentials to the Projector Augmented-Wave Method*, *Phys. Rev. B* **59**, 1758 (1999).
- [58] G. Kresse and J. Furthmüller, *Efficient Iterative Schemes for Ab Initio Total-Energy Calculations Using a Plane-Wave Basis Set*, *Phys. Rev. B* **54**, 11169 (1996).
- [59] P. Giannozzi, S. Baroni, N. Bonini, M. Calandra, R. Car, C. Cavazzoni, D. Ceresoli, G.L. Chiarotti, M. Cococcioni, I. Dabo *et al.*, *QUANTUM ESPRESSO: A Modular and Open-Source Software Project for Quantum Simulations of Materials*, *J. Phys. Condens. Matter* **21**, 395502 (2009).
- [60] K. Lee, E. D. Murray, L. Kong, B. I. Lundqvist, and D. C. Langreth, *Higher-Accuracy van der Waals Density Functional*, *Phys. Rev. B* **82**, 081101(R) (2010).
- [61] M. Dion, H. Rydberg, E. Schroder, D.C. Langreth, and B.I. Lundqvist, *van der Waals Density Functional for General Geometries*, *Phys. Rev. Lett.* **92**, 246401 (2004).
- [62] J. Klimes, D. R. Bowler, and A. Michaelides, *van der Waals Density Functionals Applied to Solids*, *Phys. Rev. B* **83**, 195131 (2011).
- [63] J. Klimes, D. R. Bowler, and A. Michaelides, *Chemical Accuracy for the van der Waals Density Functional*, *J. Phys. Condens. Matter* **22**, 022201 (2010).
- [64] S. Baroni, S. D. Gironcoli, and A. D. Corso, *Phonons and Related Crystal Properties from Density-Functional Perturbation Theory*, *Rev. Mod. Phys.* **73**, 515 (2001).

*Correction:* The ordering of the support statements in the Acknowledgments section was presented incorrectly and has been fixed.